
Article:
Li, X orcid.org/0000-0002-1536-4195, Kang, LI, Xiao, E et al. (2 more authors) (2020) Real-time peak power prediction for zinc nickel single flow batteries. Journal of Power Sources, 448. 227346. ISSN 0378-7753

https://doi.org/10.1016/j.jpowsour.2019.227346

Real-time peak power prediction for zinc nickel single flow batteries

Shawn LI[a], Kang LI[a,*], Evan XIAO[b], Jianhua ZHANG[c], Min ZHENG[d]

[a]*School of Electronic and Electric Engineering, University of Leeds, LS2 9JT, UK*
[b]*Department of Mathematical Sciences, Tsinghua University, Beijing 100084, P. R. China.*
[c]*The State Key Laboratory of Alternate Electrical Power System with Renewable Energy Sources, North China Electric Power University, Beijing 102206, P. R. China*
[d]*School of Mechatronic Engineering and Automation, Shanghai University, Shanghai 20072, P. R. China*

Abstract

The Zinc Nickel single flow batteries (ZNBs) have gained increasing attention recently. Due to the high variability of the intermittent renewable energy sources, load demands, and the operating conditions, the state of charge (SoC) is not an ideal indicator to gauge the potential cycling abilities. Alternatively, the peak power is more closely related to the instantaneous power acceptance and deliverance, and its real-time estimation plays a key role in grid-based energy storage systems. However, little has been done to comprehensively examine the peak power delivery capability of Zinc Nickel single flow batteries (ZNBs). To fill this gap, the recursive least square (RLS) method is first employed to achieve online battery model identification and represent the impact of varying operation conditions. The state of charge (SoC) is then estimated by the extended Kalman filter (EKF). With these preliminaries, a novel peak power prediction method is developed based on rolling prediction horizon. Four indices are proposed to capture the characteristics of the peak power capability over length-varying prediction windows. Finally, the consequent impact of the electrode material and applied flow rate on peak power deliverability are analysed qualitatively.

Keywords: online model identification, real-time estimation, peak power prediction, zinc nickel single assisted flow batteries

*Corresponding author
Email addresses: elxli@leeds.ac.uk (Shawn LI), k.li1@leeds.ac.uk (Kang LI), zjhncepu@163.com (Jianhua ZHANG)

1. Introduction

The redox flow batteries (RFBs) have been widely deployed as an energy storage system in the utility grids worldwide at MWh scale to support the load levelling, power quality control, supply security, and renewable energy acceptance [1, 2, 3]. A standard RFBs system consists of two modules to separate the abilities of meeting the power and energy requirements respectively [4]. Two external reservoirs are employed to store the aqueously electroactive electrolytes which convert the chemical energy into electricity. A sequence of individual cells are stacked in parallel to provide the power capacities. Thereby, the energy and power modules of RFBs are completely split by the structural merits. In this regard, an outstanding feature of RBFs is that battery capacities will increase with the concentration and volume of the applied soluble redox couples [1, 4, 5, 3]. While for a single cell, an ion-membrane separator is sandwiched in the middle of two electrodes, and electrolytes are circularly driven by two independently auxiliary pumps. The relatively simple construction will lead to straightforward scaled-up. There are three widely accepted and well investigated RBF systems, namely the polysulphide bromine [6], all vanadium [7] and zinc bromine redox flow batteries [8]. Although these RBFs have gained substantial interest in grid applications, the relatively high costs of the ion-membranes and the interference of the electrolyte cross-contamination are still the main bottlenecks for their future development [4]. Single flow battery technique was first exploited by Pletcher [9]. This favourable system breaks through the aforementioned limitations and only one flow passenger (electrolyte) is employed to remarkably simplify the construction, while the often expensive ion-membranes are not required in the system design, and the cross-contamination is thus eliminated. The zinc nickel single flow batteries (ZNBs) proposed by Cheng [10] is a new single flow battery for which the zincate is dissolved in the high concentration potassium hydroxide medium. In the charging phase, zinc is electrodeposited from the zincate ions at the negative electrode and $Ni(OH)_2$ is oxidised to $NiOOH$ at the positive electrodes, and vice versa [11]. In comparisons of other RFBs, ZNBs exhibit the promising features in terms of its intrinsic higher specific energy (with theoretical electromotive force up to $1.70V$), abundant and nontoxic

materials of redox couples (reducing environmental impact), and nonflammable supporting electrolyte (safe and dependable utilisation) [10, 11, 12]. In short, due to a number of merits, such as low cost and material abundance of its redox couples, environment-friendly chemistries, relatively high standard electrode potential, and desirable power and energy densities, the development of ZNBs technique is attractive. However, due to the inherent surface conversion and relatively poor kinetics in the positive reaction, the internal redox reaction shows a polarisation proneness during the normal cycling of ZNBs [13]. As a consequence, the gas evolution often accompanies with the positive reaction [14] and battery performance is compromised at the high charge rate tests [15]. Therefore, a reliable battery management system (BMS) is essential to operate ZNBs within the safe bounds and to provide the information of the in-situ states concurrently, before any practical application becomes feasible.

The peak power capability is an instantaneous state relating to the loading capacity in battery applications [16, 17, 18]. It can be interpreted by the maximum remaining abilities of a battery to meet the subsequent power demands [19, 20]. Analogous to the remaining fuel in the fuel tank of an internal combustion (IC) engine, the state of charge (SoC) of a battery only represents the ratio of the residual charges in a specific operating point to the normal capacity. Relying only on such knowledge, it is still not possible to know exactly how much power or peak power can be drawn from the battery. As a grid-tied energy storage system, it is imperative to know its absorbing and delivering limitations at time-varying working conditions. For instance, in the renewable energy market [21], the state information of peak power capability will assist the system operator to regulate the amount of battery absorption/delivery power in response to the instantaneous changes in supply and demand, and to abnormal operation conditions. For instance, the information of peak power capacity is critical to protect the battery stack when the instantly excessive generation from renewable power by wind turbines and solar panels greater than the its accepting potential (peak power) of energy storage systems. Thereby, an accurate prediction of the peak power capability is pivotal for safely and reliably operating the grid-based energy storage systems such as ZNBs.

To the best of our knowledge, substantial research has been conducted on the development of new materials and chemistries for ZNBs [15, 22, 23, 14, 13, 24]. However, little study has been done so far on the ZNBs management and optimising the performance from the application perspectives. The essence of peak power prediction is to render the value of maximum power in a short-term without violating the safe operating area (SoA) [18]. Over the past decades, the hybrid pulse power characterisation tests (HPPC) are broadly adopted in the lithium batteries online tests [25]. HPPC tests at once were also considered for other electrical accumulators like all-vanadium redox flow batteries (VRBs). The research of [26] reports the temperature dependency in the peak power prediction. However, the HPPC method restrains the magnitudes of terminal voltages. The HPPC based peak power prediction is thus flawed due to the absence of constraints imposed on the SoC, leading to the overoptimistic prediction at higher and lower SoC segments. In addition, the HPPC prediction fails to consider the effects of increasing resistance at the low SoC segments. Overpredictions will be problematic for the battery operation as it may result in overcharging/discharging peoblems [27]. In contrast, the model based peak power prediction is more reliable and effective [28, 17]. With the merits of the real time identification, the uncertainties arising from the varying conditions will be addressed easily. Furthermore, due to its access to the battery internal states such as the SoC, various factors contributing to accurate peak power predictions, such as SOC, design limitations, voltage and flow, will be incorporated. To achieve accurate predictions, a suitable battery model is indispensable.

A number of model types have been proposed in the literature, examples include electrochemical models, equivalent circuit model (ECM), data driven model, etc. [29]. While for real time applications, the ECM models are among the most popular ones. In [30], 12 battery models are compared, the first-order RC model is claimed to be the best candidate for $LiFePO4$ cells. Yet, the best model to characterise the electrochemical behaviours of ZNBs is still an area to be investigated. Whereas, substantial research has confirmed that the ECM based battery modelling techniques and its variants exhibit some distinctive merits of exceptional adaptability, easy implementation and desirable accuracy, and thus it is a promising candidate for the onboard studies [19]. In [20] and [31], a first order ECM model

is adopted to achieve accurate peak power predication in short-term prediction horizons. While, [32] and [16] improved the model by integrating the thermal model with the ECM to ensure the model fidelity and investigating the current dependency of the internal resistance, respectively. Analogously, Zhang [33] proposed an ECM model taking into account of the ion diffusion process. However, the offline model training is highly dependent on the experimental dataset and is not online adaptable. The performance can be significantly deteriorated for given unseen data. Recently, Wei et al [31] investigated the peak power prediction of VRBs. The peak power predictions are made over different prediction horizons, which is regarded as the benchmarks for RFBs. However, a common drawback of the state-of-the-art methods is that the terminal current signal applied across the predictive horizon is assumed to be a constant value. Thereby, the correlation between terminal signals in terms of current and voltage is assumed to be rigorously monotonous. The peak power prediction is thus converted to a problem of how to ascertain the peak current while the peak current is solved from a set of equality constraints. However, in reality, the terminal signals (current/voltage) are time-varying and highly dynamic. To overcome the drawbacks, the first-order ECM based state space model and the broadly accepted recursive least square (RLS) method are adopted in this paper to capture the battery dynamics and update the model parameters in real time. Then the SoC is estimated online by the Extended Kalman filter (EKF). With these preliminaries, the peak power prediction of ZNBs is achieved online using the prediction horizon concept where the prediction of peak power is calculated in the range from $1s$ to $20s$ [34] with the assistance of the linear programming technique. Further, in addition to the peak power, three plus indices, namely the the peak current, peak terminal voltage, and peak SoC, are designed to render the user-end comprehensive insights into the information of peak power against various prediction horizons. Finally, the additional current bounds due to the influences of material and flow rates are discussed as a supplementary discussion.

The remainder of the paper is organised as follows. Section 2 introduces the ECM based battery model and the online identification process as well as the EKF based SoC estimation. The online peak power prediction and the corresponding constraints are given in Section 3. Section 4 presents the experimental settings and procedures. Section 5 analyses

the resultant peak power predictions, which confirms the effectiveness and efficiency of the proposed methods. Section 6 concludes the paper.

2. Adaptive battery model identification and SoC estimation

2.1. Equivalent circuit model

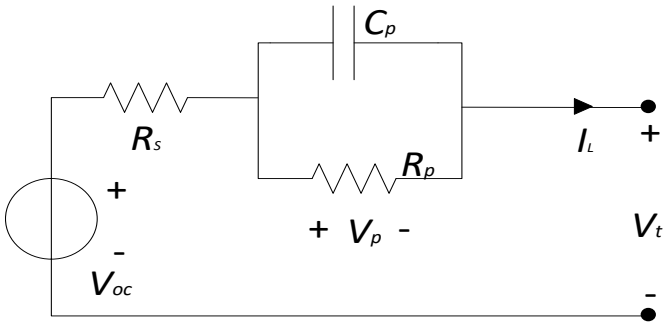

(a) First order RC Equivalent circuit model

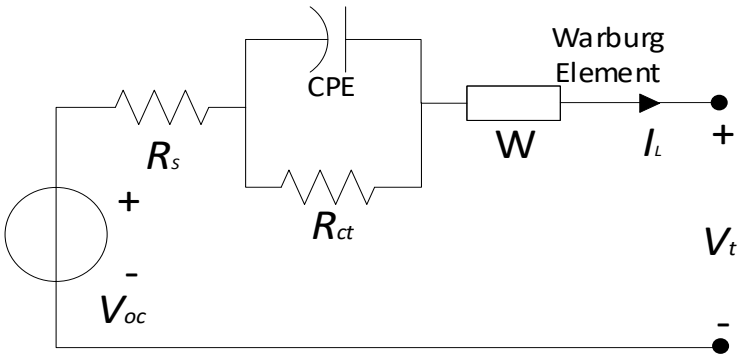

(b) Equivalent circuit of the impedance model

Figure 1: Typical equivalent circuit models (ECM): a) the commonly adopted first order ECM model when being used for online application and b) the impedance modeling based on fractional-order circuit models

The equivalent circuit models (ECMs) based battery characterisation techniques are considered as one of the most efficient methods to reproduce the dynamic process of the electrochemical system. At this point, researches have been conducted to correlate the experimental measurements with certain electrical elements, e.g. lumped resistors, capacitors,

indicators, and voltage sources [30, 35]. Fig.1(a) and Fig.1(b) shows two widely adopted ECM architectures for different applications, where a typical impedance model (IM) is given in Fig.1(b). In this regards, a Warburg impedance Z_W is employed in the circuit to elucidate the dynamics of mass transports during the slow diffusion process, and then the constant phase element (CPE) and resistor are connected in parallel to represent the dynamic characterises in charges transports. However, in such an IM, the load dynamics corresponding to the demanding variations are not taken into consideration, since the IMs are developed to achieve more accurate cell modelling in a full frequency range [36]. Besides, the parameters of IM are pre-identified through the the certain impedance spectra under specified state of charge (SoC) and ambient temperature, which are subject to significant changes as the temperature varies [35]. Meanwhile, due to the high complexity of the IM, it introduces extra difficulty in battery modeling and state estimations for online applications.

On the other hand, compared with IM, the simplified architecture of ECM with the first order RC circuit is routinely considered for the real-time application. As shown in Fig.1(a), the charge-transfer kinetics are characterised by the RC circuit with a specific time constant. Generally, the higher order RC circuit models increase the accuracy, for example, in [36], 5th order RC circuit model is shown to produce similar results in line with the impedance modeling. However, to choose a suitable EMC model is a comprise between the computational effort and numerical instability. Based on the studies in [30], the first-order ECM is an acceptable trade-off for battery modelling in reproducing the transient and dynamic performances in most cases. Additionally, the first-order ECM is able to simplify the filter design for the state estimation to attenuate the cross-interference in the estimations from the higher dimensions. Accordingly, the first-order ECM is used in this work. The schematic diagram is illustrated in Fig.1(a). In this regard, R_s is the ohmic resistance stands for the resistant losses in the electrodes and electrolyte phases. The parallel RC branch mimics the electrochemical behaviours of the ZNBs in terms of the transient responses and relaxation effects. R_p and C_p represents the polarisation resistance and capacitance, respectively. The terminal current and voltage signals are denoted by I_L and V_t. When the battery is disconnected from the circuit, the terminal voltage will

gradually converge to the equilibrium value denoted as V_{oc}.

2.2. Online model parameter identification

Herein, the charging current is predefined as the negative sign, and vice versa. In the basis of the RC responses, the first order equivalent electric circuit model can be then expressed as follows:

$$C_p \frac{dV_p}{dt} + \frac{V_p}{R_p} = I_L \tag{1}$$

$$V_t = V_{OC} - V_p - I_L R_s \tag{2}$$

the discrete-time expression of Eq (1) is of the form:

$$V_p(t) = e^{-\frac{\Delta t_s}{R_p C_p}} V_p(t - \Delta t_s) + \left(1 - e^{-\frac{\Delta t_s}{R_p C_p}}\right) R_p I_L(t - \Delta t_s) \tag{3}$$

where the start-up time is 0, and Δt_s denotes a fixed time interval. Define $V_p(k) = V_p(k\Delta t_s)$ and the analogous definitions are imposed on V_{OC}, V_t, and I_L. A neat format is given as follows:

$$V_p(k) = e^{-\frac{\Delta t_s}{R_p C_p}} V_p(k-1) + \left(1 - e^{-\frac{\Delta t_s}{R_p C_p}}\right) R_p I_L(k-1) \tag{4}$$

According to Eq (2), substituting $V_p = V_{OC} - V_t - I_L R_s$ to Eq (4), the expression of $V_t(k)$ is yielded as:

$$\begin{aligned} V_t(k) = \beta V_t(k-1) - R_s I_L(k) + (\beta \cdot R_s - (1-\beta)R_p) I_L(k-1) \\ + \left(V_{OC}(k) - \beta V_{OC}(k-1)\right), \end{aligned} \tag{5}$$

where $\beta = e^{-\frac{\Delta t_s}{R_p C_p}}$. One time step difference is introduced to Eq (5), the differential voltage of V_t is given as:

$$\begin{aligned} \Delta V_t(k) = \beta \Delta V_t(k-1) - R_s \Delta I_L(k) + (\beta \cdot R_s - (1-\beta)R_p) \Delta I_L(k-1) \\ + \left(\Delta V_{OC}(k) - \beta \Delta V_{OC}(k-1)\right) \end{aligned} \tag{6}$$

where the last term $(\Delta V_{OC}(k) - \beta \Delta V_{OC}(k-1))$ is treated as the error term, denoted as $e(k)$, due to the slow varying OCV in the ZNBs. In this regard, the regression formula is expressed as:

$$h(k) = \theta^T(k)\phi(k) + e(k), \tag{7}$$

where

$$h(k) = \Delta V_t(k), \quad \theta(k) = \boldsymbol{\alpha} = [\alpha_1, \quad \alpha_2, \quad \alpha_3]^T = [\beta, \quad -R_s, \quad (\beta \cdot R_s - (1-\beta)R_p)]^T,$$
$$\phi(k) = [\Delta V_t(k-1), \Delta I_L(k), \Delta I_L(k-1)]^T, \quad e(k) = \Delta V_{OC}(k) - \alpha_1 \Delta V_{OC}(k-1). \tag{8}$$

The RLS method [31] is employed to estimate $\theta(k)$ recursively. After obtaining $\hat{\theta}(k)$, the model parameters $[\hat{R}_s, \hat{R}_p, \hat{C}_p]^T$ can be reversely derived by:

$$\begin{aligned}
\hat{R}_s &= -\hat{\alpha}_2, \quad \hat{\beta} = \hat{\alpha}_1, \\
\hat{R}_p &= \frac{\hat{\beta} \cdot \hat{R}_s - \hat{\alpha}_3}{1 - \hat{\beta}} = \frac{-\hat{\alpha}_1 \hat{\alpha}_2 - \hat{\alpha}_3}{1 - \hat{\alpha}_1}, \\
\hat{C}_p &= -\frac{\Delta t_s}{\hat{R}_p \log(\hat{\beta})} = \frac{\Delta t_s \cdot (1 - \hat{\alpha}_1)}{(\hat{\alpha}_1 \hat{\alpha}_2 + \hat{\alpha}_3) \log(\hat{\alpha}_1)}.
\end{aligned}$$

Assuming independent and identically distributed (i.i.d.) measurement noise, differential treatment further transforms the errors into zero-mean and symmetrically distributed. Hence, constant term explaining the bias is not needed in 7. Note that this modelling error may not necessarily be a Gaussian noise sequence globally, but given the differential treatment in formulating the regression equation and utilization of the forgetting factors in RLS, the Direct Current (DC) bias is significantly attenuated, so as for any bias introduced into the model parameter estimation, which has be further verified in the experimental section.

In RLS, the forgetting factor $\lambda = 0.98$ is used. Meanwhile, in order to smooth the fluctuations in these variables at different time scales, the multi-timescale RLS algorithm [37] is adopted in the identification process, where the sample rate for R_s is set as $1s$, oppositely, $4s$ are sampling time is used for both V_p and C_p. Note that the ZNBs is a slow time-varying system, and different electrical elements have different convergence speeds. In this regard, the multi-time scale RLS with fixed forgetting factors rather than other methods is employed for the online parameter identification. While we noticed that other methods produce poor modelling results due to their convergence issues.

2.3. SoC online estimation based on EKF algrothm

The state of charge (SoC) is the ratio of the remaining charge to the nominal capacity value at a specific operating condition. The Coulomb counting (CC) method is readily

implementable and reliable, but it is subject to the unknown perturbations and initial deviations [37]. Additionally, the SoC-OCV look-up table is an open-loop method, in which the SoC can be read straightforward from the inherent monotonous SoC-OCV table. Nevertheless, the pre-trained SoC-OCV table has to be calibrated periodically, due to the effects of the battery degradation. Additionally, the measurement noises and uncertainties introduced into the model are still not dealt with appropriately. As a widely accepted method, the extended Kalman filter (EKF) estimates the SoC values in a closed-loop manner and dynamically filter out the measurement noises and uncertainties introduced into the SOC estimation compared with the open-loop method. Based on Eq (4), a two-dimensional state equation can be derived as:

$$\begin{cases} SoC(k) = SoC(k-1) - \frac{\eta \Delta t_s}{Q} I_L(k-1) \\ V_p(k) = e^{-\frac{\Delta t_s}{R_p C_p}} V_p(k-1) + \left(1 - e^{-\frac{\Delta t_s}{R_p C_p}}\right) R_p I_L(k-1) \end{cases} \tag{9}$$

The terminal voltage signal V_t is formulated as the measurement equation:

$$V_t(k) = f(SoC(k)) - V_p(k) - R_s I_L(k) \tag{10}$$

where $V_{OC} = f(SoC)$. Therein, the incremental OCV tests (IO) [25, 38] are conducted to formulate the SoC-OCV table. According to the IO method, the ZNB cell stack is charged under the constant current constant voltage (CCCV) regime. Afterwards, the fully charged battery is then discharged by pulse current in order to drain up the its capacity. Throughout the experiments, the SoC values are recorded by high precision current sensors based on the coulomb counting (CC) method. Meanwhile, the OCV values are logged at the end of each discharging interval. Finally, the SoC-OCV relationship is characterized by the averaging three current profiles in terms of $0.5C(1.85A)$, $1C(3.70A)$, and $1.5C(5.55A)$. At this point, f is calibrated as a fifth-order polynomial [39], which correlates the relationship between OCV and SoC. Follow-on, a standard expression of EKF is then formulated as:

$$\begin{cases} \mathbf{s}(k) = \mathbf{A}_k \cdot \mathbf{s}(k-1) + \boldsymbol{b}_k \cdot I_L(k-1) + \mathrm{w}(k) \\ V_t(k) = F(\mathbf{s}(k), I_L(k)) + \mathrm{v}(k) \end{cases} \tag{11}$$

where

$$\mathbf{s}(k) = [SoC(k) \quad V_p(k)]^T, \quad \mathbf{A}_k = \begin{bmatrix} 1 & 0 \\ 0 & e^{-\frac{\Delta t_s}{R_p C_p}} \end{bmatrix},$$
$$\boldsymbol{b}_k = \begin{bmatrix} -\frac{\eta \Delta t_s}{Q} & (1 - e^{-\frac{\Delta t_s}{R_p C_p}}) R_p \end{bmatrix}^T,$$
$$F(\mathbf{s}, I) = f(s_1) - s_2 - R_s I, \quad \frac{\partial F}{\partial \mathbf{s}} = [f'(s_1) \quad -1].$$

w(k) and v(k) are the process noise and the measurement noise respectively, which are assumed to be independent, zero-mean, Gaussian noise processes with covariance matrices $\sum_w$ and $\sum_v$. In this respect, the discrete-time prediction and update equations of EKF are summarized as follows:

Prediction

$$\hat{\mathbf{s}}^-(k) = \mathbf{A}_k \cdot \hat{\mathbf{s}}^+(k-1) + \boldsymbol{b}_k \cdot I_L(k-1)$$
$$\hat{\Sigma}_{\mathbf{s}}^-(k) = \mathbf{A}_k \hat{\Sigma}_{\mathbf{s}}^+(k-1) \mathbf{A}_k^T + \Sigma_w$$

Update

$$e(k) = V_t(k) - F(\hat{\mathbf{s}}^-(k), I_L(k))$$
$$\mathbf{L}_k = \hat{\Sigma}_{\mathbf{s}}^-(k) \mathbf{H}_k^T \left[\mathbf{H}_k \hat{\Sigma}_{\mathbf{s}}^-(k) \mathbf{H}_k^T + \Sigma_v \right]^{-1}$$
$$\hat{\mathbf{s}}^+(k) = \hat{\mathbf{s}}^-(k) + \mathbf{L}_k \cdot e(k)$$
$$\hat{\Sigma}_{\mathbf{s}}^+(k) = (\mathbf{I} - \mathbf{L}_k \cdot \mathbf{H}_k) \hat{\Sigma}_{\mathbf{s}}^-(k)$$

Define

$$\mathbf{A}_k = \begin{bmatrix} 1 & 0 \\ 0 & \hat{\beta} \end{bmatrix},$$
$$\mathbf{H}_k = \frac{\partial F(\mathbf{s}, I_L(k))}{\partial \mathbf{s}}|_{\mathbf{s}=\hat{\mathbf{s}}^-(k)} = [f'(\hat{SoC}^-(k)) \quad -1] \tag{12}$$

where $\hat{\beta}$ is the identified parameter in Eq (7) and Eq (8), and the superscripts $^-$ and $^+$ denote the priori state update and posterior state update phases respectively. For the details of the EKF based SoC estimation adoped in this work, please refer to [40].

3. Online peak power prediction

Motivated by the receding horizon concept in model predictive control that has been widely adopted in process industry [41, 42], a moving horizon scheme for peak power prediction is proposed in this paper. This method handles the dynamics of the current and voltage within the prediction window, where the discharging and charging current is not assumed to be constant. Similar to the MPC [42] strategy, the constraints could be explicitly formulated in the peak power prediction equations, and constraints on the terminal voltage, SoC, flow effects, and electrode material limitation can all be included. This approach can thus easily search the optimum by solving linear programming problems, whilst taking all the constraints into the optimisation process. If one variable reaches to its constraint, the discharging and charging current in the prediction horizon will be fixed. In this regard, it enables the safe operations.

3.1. Battery state space model for peak power prediction

Due to the implicit relationship between SoC and current I_L, the CC method can be expressed as:

$$SoC_k = SoC_{k-1} - \frac{\eta I_L(k-1)\Delta t_s}{Q} \tag{13}$$

where Q denotes the slowly changing battery capacity. It should be noted as the value of Q is assumed to be constant within the first half of discharging and charging cycle. The coulombic efficiency η is set as 100% for simplification. By applying the Taylor approximation to the equation of $V_{OC} = f(SoC)$, a recursive formula for V_{OC} is yielded accordingly:

$$\begin{aligned} V_{OC}(k+i|k) &= f(SoC(k+i|k)) \approx V_{OC}(k) + f'(SoC(k))\left[SoC(k+i|k) - SoC(k)\right] \\ &= V_{OC}(k) - f'(SoC(k))\frac{\eta\Delta t_s}{Q}\sum_{j=0}^{i-1} I_L(k+j) \end{aligned} \tag{14}$$

Since the change of SoC depends on the slowly accumulating current effect, during the period of two consecutive sample instants, the values of $SoC(k+i|k)$ and $SoC(k)$ are very close. The above equation could then be reformulated as:

$$V_{OC}(k+i|k) = V_{OC}(k+i-1|k) - f'(SoC(k))\frac{\eta\Delta t_s}{Q} I_L(k+i-1) \tag{15}$$

Combined with Eq (9) and Eq (10), the battery model can be expressed in the state space form. Therefore, a three-dimensional predictive state equation system is formulated as follows:

$$\begin{cases} \mathbf{x}(k+i|k) = \mathbf{P}_k \cdot \mathbf{x}(k+i-1|k) + \boldsymbol{q}_k \cdot u(k+i-1) \\ y(k+i|k) = \mathbf{C}_k \cdot \mathbf{x}(k+i|k) + d_k \cdot u(k+i) \end{cases} \tag{16}$$

where

$$\mathbf{x}(k+i|k) = [SoC(k+i|k) \quad V_p(k+i|k) \quad V_{OC}(k+i|k)]^T,$$

$$\mathbf{P}_k = \begin{bmatrix} 1 & 0 & 0 \\ 0 & e^{-\frac{\Delta t_s}{R_p C_p}} & 0 \\ 0 & 0 & 1 \end{bmatrix}, \quad \boldsymbol{q}_k = [-\frac{\eta \Delta t_s}{Q} \quad (1 - e^{-\frac{\Delta t_s}{R_p C_p}}) R_p \quad - f'(SoC(k)) \frac{\eta \Delta t_s}{Q}]^T,$$

$$y(k+i|k) = V_t(k+i|k), \quad \mathbf{C}_k = [0 \quad -1 \quad 1]^T, \quad d_k = -R_s, \quad u(k+i) = I_L(k),$$

According the rolling horizon scheme, the prediction of the state vector and input variable (I_L) are further explained by $\mathbf{x}(k+i|k)$, and $u(k+i)$, respectively. Therefore, the neat expression of $\mathbf{x}(k+i|k)$ can be then derived as follows:

$$\mathbf{x}(k+i|k) = \mathbf{P}_k^i \cdot \mathbf{x}(k) + \sum_{j=0}^{i-1} \mathbf{P}_k^{i-1-j} \boldsymbol{q}_k \cdot u(k+j) \tag{17}$$

Impose the vector notation on the prediction state $\mathbf{x}(k+i|k)$, and Eq (17) can be then expanded over a prediction window of n steps:

$$\vec{\mathbf{x}}^{(n)}(k) = \begin{bmatrix} \mathbf{x}(k+1|k) \\ \mathbf{x}(k+2|k) \\ \vdots \\ \mathbf{x}(k+n|k) \end{bmatrix} = \mathbf{P}_k^{(n)} \cdot \mathbf{x}(k) + \mathbf{P}_{q,k}^{(n)} \cdot \begin{bmatrix} u(k) \\ u(k+1) \\ \vdots \\ u(k+n-1) \end{bmatrix} = \mathbf{A}_{x,k}^{(n)} \cdot \vec{\boldsymbol{u}}^{(n)}(k) + \boldsymbol{b}_{x,k}^{(n)} \tag{18}$$

where

$$\mathbf{P}_k^{(n)} = \begin{bmatrix} \mathbf{P}_k \\ \mathbf{P}_k^2 \\ \vdots \\ \mathbf{P}_k^n \end{bmatrix}, \quad \mathbf{P}_{q,k}^{(n)} = \begin{bmatrix} \boldsymbol{q}_k & \mathbf{0} & \cdots & \mathbf{0} \\ \mathbf{P}_k \cdot \boldsymbol{q}_k & \boldsymbol{q}_k & \cdots & \mathbf{0} \\ \vdots & \vdots & \vdots & \vdots \\ \mathbf{P}_k^{n-1} \cdot \boldsymbol{q}_k & \mathbf{P}_k^{m-2} \cdot \boldsymbol{q}_k & \cdots & \boldsymbol{q}_k \end{bmatrix}, \quad \vec{\boldsymbol{u}}^{(n)}(k) = \begin{bmatrix} u(k+1) \\ u(k+2) \\ \vdots \\ u(k+n) \end{bmatrix},$$

$$\mathbf{A}_{x,k}^{(n)} = \mathbf{P}_{q,k}^{(n)} \cdot \begin{bmatrix} \mathbf{0} & \mathbf{0} \\ \boldsymbol{I}_{n-1} & \mathbf{0} \end{bmatrix}, \quad \boldsymbol{b}_{x,k}^{(n)} = \mathbf{P}_k^{(n)} \cdot \mathbf{x}(k) + \mathbf{P}_{q,k}^{(n)} \cdot \begin{bmatrix} u(k) \\ 0 \\ \vdots \\ 0 \end{bmatrix}$$

Similarly, a set of n ahead predictions $y(k+i|k)$ can be accordingly deduced as follows:

$$\begin{aligned} \vec{\boldsymbol{y}}^{(n)}(k) &= \begin{bmatrix} y(k+1|k) \\ y(k+2|k) \\ \vdots \\ y(k+n|k) \end{bmatrix} = \begin{bmatrix} \mathbf{C}_k & \mathbf{0} & \cdots & \mathbf{0} \\ \mathbf{0} & \mathbf{C}_k & \cdots & \mathbf{0} \\ \vdots & \vdots & \vdots & \vdots \\ \mathbf{0} & \mathbf{0} & \cdots & \mathbf{C}_k \end{bmatrix} \cdot \vec{\mathbf{x}}^{(n)}(k) + \begin{bmatrix} d_k & 0 & \cdots & 0 \\ 0 & d_k & \cdots & 0 \\ \vdots & \vdots & \vdots & \vdots \\ 0 & 0 & \cdots & d_k \end{bmatrix} \cdot \vec{\boldsymbol{u}}^{(n)}(k) \\ &= \mathbf{A}_{y,k}^{(n)} \cdot \vec{\boldsymbol{u}}^{(n)}(k) + \boldsymbol{b}_{y,k}^{(n)} \end{aligned} \tag{19}$$

where

$$\begin{aligned} \mathbf{A}_{y,k}^{(n)} &= \mathrm{diag}(\mathbf{C}_k, \mathbf{C}_k, \cdots, \mathbf{C}_k) \cdot \mathbf{A}_{x,k}^{(n)} + \mathrm{diag}(d_k, d_k, \cdots, d_k), \\ \boldsymbol{b}_{y,k}^{(n)} &= \mathrm{diag}(\mathbf{C}_k, \mathbf{C}_k, \cdots, \mathbf{C}_k) \cdot \boldsymbol{b}_{x,k}^{(n)} \end{aligned}$$

Note that the peak power prediction horizon is often set within short-term view (in the range from $1s$ to $20s$). At an operating point, the RLS based model identification will be executed first to update the parameters. The model dynamics will be fully taken into the following prediction steps. Herein, the prediction window (prediction horizon) n begins from $1s$ and ends at $20s$. The imposed constraints on the voltage, SoC and current are strictly guaranteed at each prediction step.

3.2. Moving horizon scheme based optimisation

Due to the similar equation derivation and optimisation procedure for both the charging and discharging phases, only the discharging phase is selected for presentation in this section.

In this regard, the average power in the prediction window is to be maximized. In the meantime, the SoC and V_t are confined within their particularly allowable ranges. Hence, the objective function can be further interpreted as:

$$\begin{aligned} P_{peak}^{dis} &= \max_{\vec{\boldsymbol{u}}^{(n)}(k)} \frac{1}{n} \sum_{i=1}^{n} u(k+i) y(k+i|k) = \max_{\vec{\boldsymbol{u}}^{(n)}(k)} \frac{1}{n} \vec{\boldsymbol{u}}^{(n)}(k)^T \cdot \vec{\boldsymbol{y}}^{(n)}(k) \\ &= \max_{\vec{\boldsymbol{u}}^{(n)}(k)} \vec{\boldsymbol{u}}^{(n)}(k)^T \cdot \mathbf{A}_{y,k}^{(n)} \cdot \vec{\boldsymbol{u}}^{(n)}(k) + \boldsymbol{b}_{y,k}^{(n)^T} \cdot \vec{\boldsymbol{u}}^{(n)}(k) \end{aligned} \tag{20}$$

Combined with constraints on the voltage, current, and SoC, the optimization problem can be stated as follows:

$$\max_{\vec{\boldsymbol{u}}^{(n)}(k)} \frac{1}{2} \vec{\boldsymbol{u}}^{(n)}(k)^T \cdot \left(\mathbf{A}_{y,k}^{(n)} + \mathbf{A}_{y,k}^{(n)^T} \right) \cdot \vec{\boldsymbol{u}}^{(n)}(k) + \boldsymbol{b}_{y,k}^{(n)^T} \cdot \vec{\boldsymbol{u}}^{(n)}(k) \tag{21}$$

$$s.t. \quad \begin{bmatrix} V_{t,min} \\ V_{t,min} \\ \vdots \\ V_{t,min} \end{bmatrix} \leq \vec{\boldsymbol{y}}^{(n)}(k) = \mathbf{A}_{y,k}^{(n)} \cdot \vec{\boldsymbol{u}}^{(n)}(k) + \boldsymbol{b}_{y,k}^{(n)} \leq \begin{bmatrix} V_{t,max} \\ V_{t,max} \\ \vdots \\ V_{t,max} \end{bmatrix},$$

$$\begin{bmatrix} SoC_{min} \\ SoC_{min} \\ \vdots \\ SoC_{min} \end{bmatrix} \leq \mathrm{diag}(\boldsymbol{e}_1, \boldsymbol{e}_1, \cdots, \boldsymbol{e}_1) \cdot (\mathbf{A}_{x,k}^{(n)} \cdot \vec{\boldsymbol{u}}^{(n)}(k) + \boldsymbol{b}_{x,k}^{(n)}) \leq \begin{bmatrix} SoC_{max} \\ SoC_{max} \\ \vdots \\ SoC_{max} \end{bmatrix},$$

$$\begin{bmatrix} I_{L,min} \\ I_{L,min} \\ \vdots \\ I_{L,min} \end{bmatrix} \leq \vec{\boldsymbol{u}}^{(n)}(k) \leq \begin{bmatrix} I_{L,max} \\ I_{L,max} \\ \vdots \\ I_{L,max} \end{bmatrix}$$

where $\boldsymbol{e}_1 = [1 \quad 0 \quad 0]$ is a unit vector. The above problem is a convex optimization problem, as matrix $-\left(\mathbf{A}_{y,k}^{(n)} + \mathbf{A}_{y,k}^{(n)^T} \right)$ is positive definite. Consequently, it can be solved using the quadratic programming. Once the optimal solution $\vec{\boldsymbol{u}}_{opt}^{(n)}(k)$ is obtained, the peak average

power can be predicted as:

$$P_{peak}^{(n)}(k) = \frac{1}{n}\sum_{i=1}^{n} V_t(k+i|k)|_{\vec{\boldsymbol{u}}_{opt}^{(n)}(k)} \cdot u_{opt}(k+i) \tag{22}$$

In addition to the peak power, three plus indices encompassing the peak current, peak terminal voltage, and peak SoC are used jointly over a varying prediction horizon:

$$I_{L,peak}^{(n)}(k) = \frac{1}{n}\sum_{i=1}^{n} u_{opt}(k+i), \tag{23}$$

$$V_{t,peak}^{(n)}(k) = \frac{1}{n}\sum_{i=1}^{n} V_t(k+i|k)|_{\vec{\boldsymbol{u}}_{opt}^{(n)}(k)}, \tag{24}$$

$$SoC_{peak}^{(n)} = \frac{1}{n}\sum_{i=1}^{n} SoC(k+i|k)|_{\vec{\boldsymbol{u}}_{opt}^{(n)}(k)} \tag{25}$$

This above elaborated approach makes full use of the dynamic correlations between current and voltage, while the amplitude of the future current does not have to be a constant, an assumption imposed by the existing approaches. Further, the over-optimistic and over-pessimistic predictions are avoided, rendering reliable and safe operations in the future. Compared with the existing methods, the predictions of the peak power at each instant SoC state are solved simply by the linear programming. The average peak power prediction presents the power limit in the corresponding prediction horizon, and all other peak power predictions over the relative prediction horizon can then be discounted. The computational cost of the proposed method is also competitive for online applications, in comparison with the existing methods.

4. Experiment and Setups

Based on the previous research [10, 12], a ZNB prototype has been made and tested in this study. The schematic of the experimental apparatus and the testing platform are illustrated in Fig.2. Four sintered nickel oxide plates (Jiangsu Highstar Battery Manufacturing) are used as the nickel electrodes (positive/cathodes electrode) and three inert electrodes such as the polished stainless steel sheets are adopted as the zinc electrodes (negative/anodes electrode). The electrodes in such a stack are connected electrically in parallel. As depicted in Fig.2, the

electrodes have been sized as $7cm * 7cm$ with a $1cm$ rectangular clip outside. All the clips are well arranged and attached together as the current collector on one side of the battery. The similar arrangement has been made on the opposite side. This arrangement results in around a voltage of $1.6V$ OCV of the cell stack. The acrylic spacers have been machined with identical scale and then sandwiched between the positive and negative electrodes. The inserted spacers prevent the electrode materials from warping and deformation. In order to render an optimal flow channel, the spacers have the thickness $5mm$ and carved with the grids based design. For leakproof, the spacer borders are encircled with gaskets. The rating capacity of ZNBs demonstrator is about $3700mAh$ defined by the amount of activated area and the material energy density. The electrolyte reservoir is made of commodity polymer for the alkaline zinc electrolyte. Regarding the preparation of electrolyte, $1Mol\ ZnO$ and $20g/L\ LiOH$ are dissolved by the $10Mol/L\ KOH$ support solution as the used electrolyte. The operating flow rate is remained at $19cm/s$. The NEWARE $CT-3008W$ is used to load the testing current profiles into the ZNBs and measure the output signals from the terminals. The measurement ranges of voltage and current are $15V$ and $3A$, respectively, and nominal measurement error bounds are within 0.1%. Throughout experiments, the ambient temperature is maintained at $25 \pm 3°C$. An external host computer is connected with the battery tester system (BTS) to log the experimental data in real time.

The ZNBs stack is cycling with the constant power regime, which is commonly adopted in the flow battery tests. For the sake of gauging the maximum discharging capabilities, the battery stack is cycling with the nominal capacity $3700mAh$ for each charging phase. Specifically, a regular cell test protocol (galvanostatic cycling) with a moderate $1C$ $(3.70A)$ constant current is imposed to feed $3700mAh$ to the cell in each charging phase, and the discharging phase will be terminated until V_t drops to the cut-off value $1.2V$. The testing data will be used for the RLS based model identification in real time. For the sake of comparison, the SoC trajectory is recorded by the coulomb counting method. Furthermore, the proposed methods provide the instantaneous prediction purely relying on the correlation between terminal signals e.g. current and voltage, it promises the abilities to be generalised for other batteries counterparts.

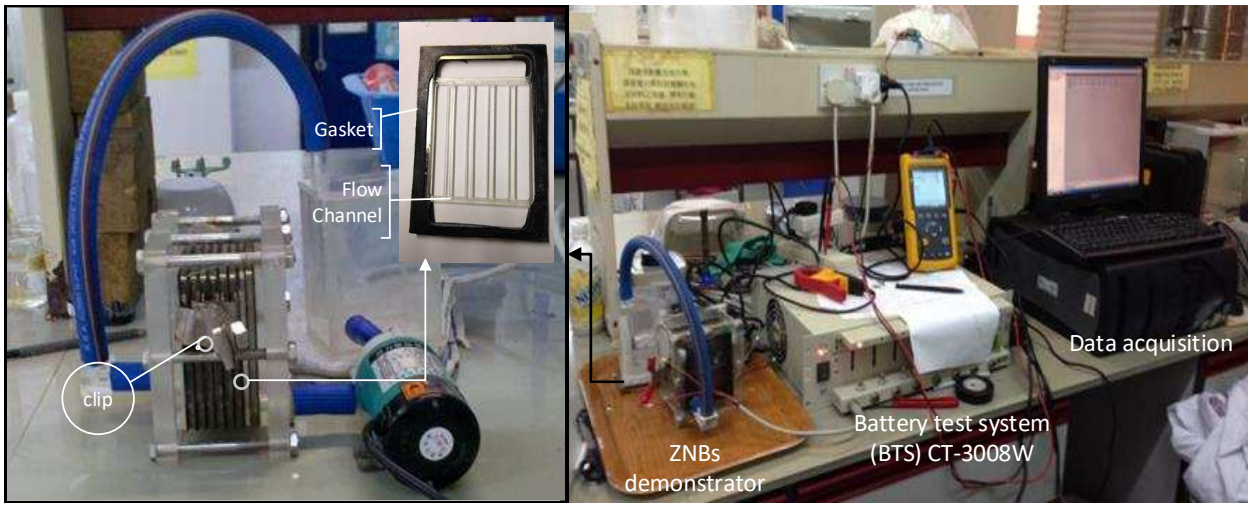

Figure 2: Showcase of the experimental platform

5. Experimental Results and Peak Power Prediction

5.1. Model verification

The accurate modelling of the battery electrical dynamics is fundamental for the peak power prediction. Additionally, since the SoC can not be accurately measured online by existing sensor techniques, the SoC estimation is fused into the model identification process. Thereby, the accurate battery model not only reproduces the dynamics in charging and discharging processes and reflects the real-time operating condition but also affirms the fidelity of SoC estimation. Fig.3 illustrates the results of EKF based SoC estimation and RLS online model identification. As no prior knowledge is available on the model parameters, the parameters are erroneously initialised as $R_s = R_p = 0.01\Omega$ and $C_p = 1000F$. It is apparent that the model matches the measured terminal voltage in the entire experiments and the error bounds are stabilised less than $0.01V$. The relatively large error spikes can be observed at the start-up point only, due to the intently erroneous initialisation. However, it converges to the reference value quickly within $5s$. The similar pattern is revealed in the SoC estimation. The estimation errors are limited to 1% throughout the tests, which manifests the effectiveness and accuracy of the synthesised RLS based real time SoC estimation approach. Additionally, through the online adaption technique, the influence of the varying

ambient environment changes can be easily taken into full consideration. Therefore, the periodic calibration of battery model can be revoked.

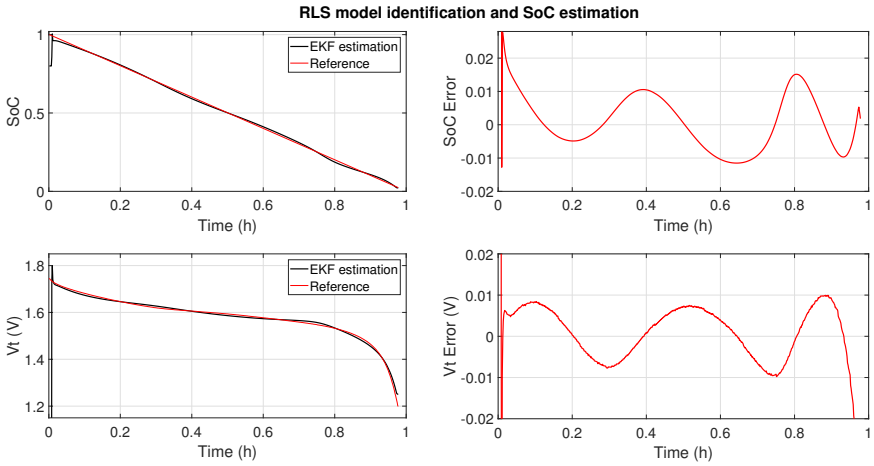

Figure 3: Model identification and SoC estimation

5.2. Peak power prediction considering both voltage and SoC constraints

The loaded current and applied flow rate play an important role in shaping the behaviours of ZNBs. However, they are not only limited by the microscopic reactions on the electrodes such as the mass transfer and ion immigration but also by the selected materials due to side reactions and zinc deposition formation. For the sake of simplification, the effects of flow rate will be decoupled from the cut-off voltage and operating SoC constraints, and it has been discussed separately in section 5.3

The ZNBs are favourable energy storage systems, which have a very high energy and power densities explained by a desirably practical range of operating voltage and SoC. In the literature [10, 12], ZNB is able to tolerate the broad scope of operating SoC (from 0 to 100%) and voltage (from $0.8V$ to $2.05V$). Imposing the voltage and SoC restraints on the ZNBs, the predicted peak power value over different prediction windows is shown in Fig.4(a). And Fig.4(b) illustrates the thorough predictions at three selected SoC states. Since the almost identical mechanism and constraints are employed for charging and discharging, in this paper, only the prediction results at the discharging phase are detailed.

Four different indices in terms of the peak current, peak SoC, peak voltage and peak power are introduced to give a comprehensive assessment of the predictions over different prediction windows. Furthermore, these four indices as a whole depict the maximum power supplying capability at the different SoC states.

5.2.1. Discharging Phase

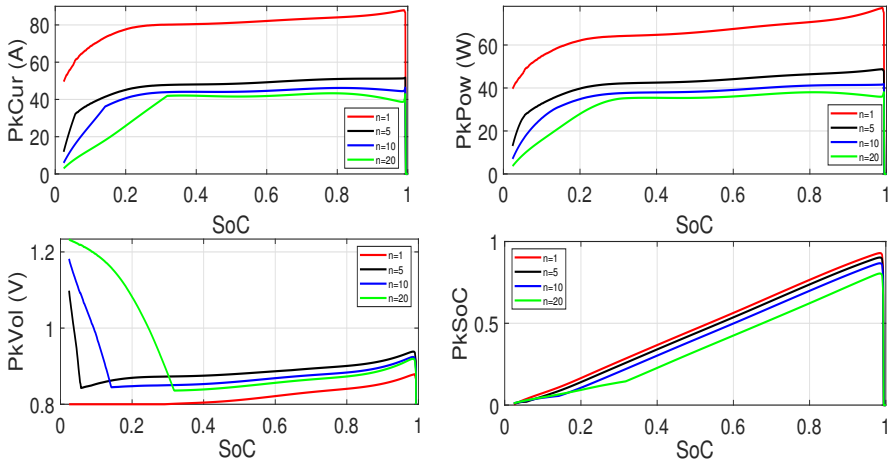

(a) Peak power prediction along the discharging process

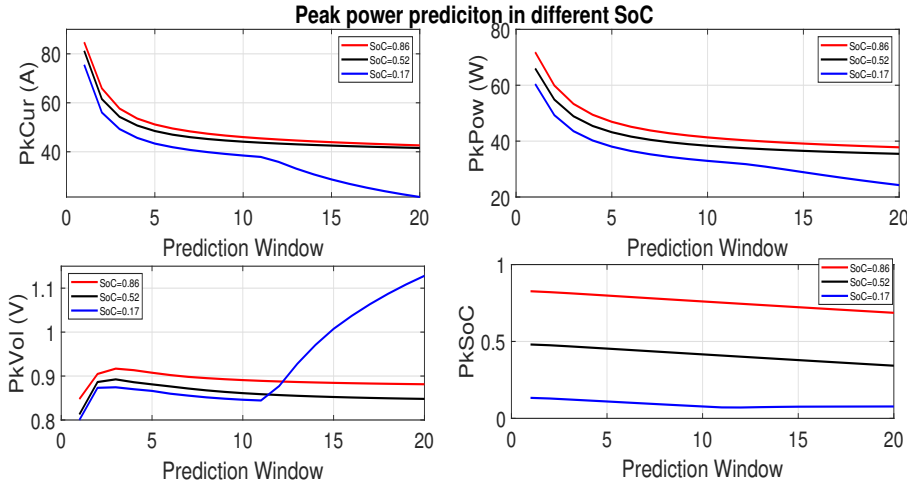

(b) Peak power prediction against different SoC states in the discharging process

Figure 4: Peak power prediction for discharging process

Fig.4(a) and Fig.4(b) show the dynamics of constraint variables along discharging process

over different prediction windows. There are four main observations which can be inferred from these subplots:

1. **The proposed ZNBs system processes highly desirable peak power deliverability over the entire discharging process.** As illustrated in the second subplot of Fig.4(a), for the majority of the operating time, the peak power prediction will stay at $38W$ for this small ZNB prototype ($3.7Ah$). Specifically, in the lower SoC ranges (0.17) as shown in the second subplot of Fig.4(b), the peak power deliverability still maintains over $20W$, where this observation also reveals that ZNBs are very promising energy storage systems amongst all kinds of defined RFBs.

2. **The constraints on peak voltage and SoC are complementary, which alternatively affect the peak power predictions.** By inspections from the third and fourth subplots of Fig.4(a), the turn points represent the timing when the control modes are switched from cut-off voltage control to SoC control. However, it has to be noted that the cut-off voltage constraint is only applicable, when the prediction window comes to $n = 1$, because in this case the SoC constraint only considers one time step, resulting in the extremely high discharging current (depicted in the first subplot of Fig.4(a)).

3. **The prediction results of the longer prediction window n are very sensitive to the SoC and cut-off voltage constraints.** As shown in Fig.4(a) and Fig.4(b), the proposed four indices are sketched to illustrate the changes in prediction windows, where the predicted peak values are reduced as the length of the prediction horizon increases. The instantaneous power is greater over short prediction horizons i.e. $n \leq 5$ as illustrated in the second subplot of Fig.4(b). However, as the gradual prediction window increasing, the maximal power delivered is reduced distinctively. In addition, as shown in the first and second subplots of Fig.4(b), except for the prediction horizon $n = 1$, similar patterns are evident for both the peak current and peak power prediction, where the cut-off voltage is the main constraint cross the whole discharging

phase. The third subplot of Fig.4(b) reveals that if the length of the prediction window is short, the cut-off voltage as the major applicable constraint, will dominate the predictions cross the entire discharging process. While the fourth subplot of Fig.4(b) further details the SoC constraint is only applicable when the battery is operating at a relatively lower SoC range (17%) and that the prediction window is longer than $n = 10$.

4. **For optimal operation, ZNBs are not recommended to operate at a lower SoC range.**

The above observations show that the four indices can provide a reliable and comprehensive characterisation of the predicted power delivery capability. In addition, the proposed maximal power prediction scheme can assist with optimal battery discharging operations. To further elaborate the adequacy of the four indices to characterise the power delivery capability at different SoC states, additional Fig.5 is given to illustrate the prediction results over different prediction windows. Again, the prediction results confirm the previous observations.

For short prediction windows, in order to provide the maximum power delivery, the predicted peak values are subject to the discharging cut-off voltage control. As the prediction window increases, the voltage control will give way to the SoC control, and the SoC threshold starts to dominate the predictions. As a consequence, the predicted peak power is reduced and the operation moves to the voltage and SoC control modes. These observations can be interpreted by the fact that the remaining charges in the battery are gradually drawn out by the peak discharging current over a long prediction horizon. It is further revealed that the peak current drops to the normal value for the $20s$ prediction window. Therefore, it is meaningless to adopt longer prediction horizons ($> 20s$). On the other hand, the discharging potential decreases significantly as the SoC drops, which implies that meticulous attention should be paid to the lower SoC range for the operation safety.

Fig.6 presents a zoom-in view at one predicted time instant over the $20s$ prediction horizon. By using the proposed moving windows scheme, at each time instant, 20 predicted

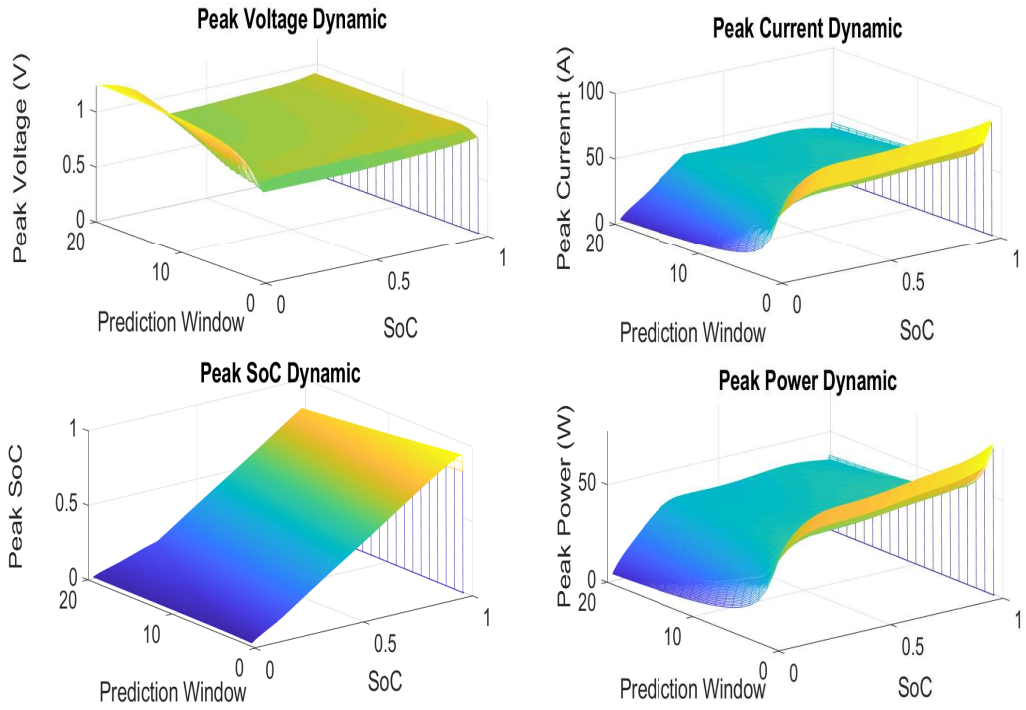

Figure 5: Peak power prediction dynamics in 3D view

discharging current values (I_L) will be produced, among which the average predicted value is regarded as the peak value in the discharging process. Unlike existing approaches, the battery dynamics are taken into account in the proposed scheme in predicting the peak power capacity within an operation window. Another remarkable feature of this method is that constraints imposed on the state variables are satisfied to maintain safe battery operation. An interesting observation is drawn from the results is that most of the predicted values of discharge currents are identical as shown in first subplot which agrees with the results obtained by other approaches presented in the literature. For different SoC states (0.86 and 0.17), it is seen inspected that a larger SoC renders a broader operating potential as revealed by the higher peak values of the four indices. While for a lower SoC state, the SoC constraint easily affects the battery operating potentials as shown in the fourth subplot and that all the four indices are reduced significantly.

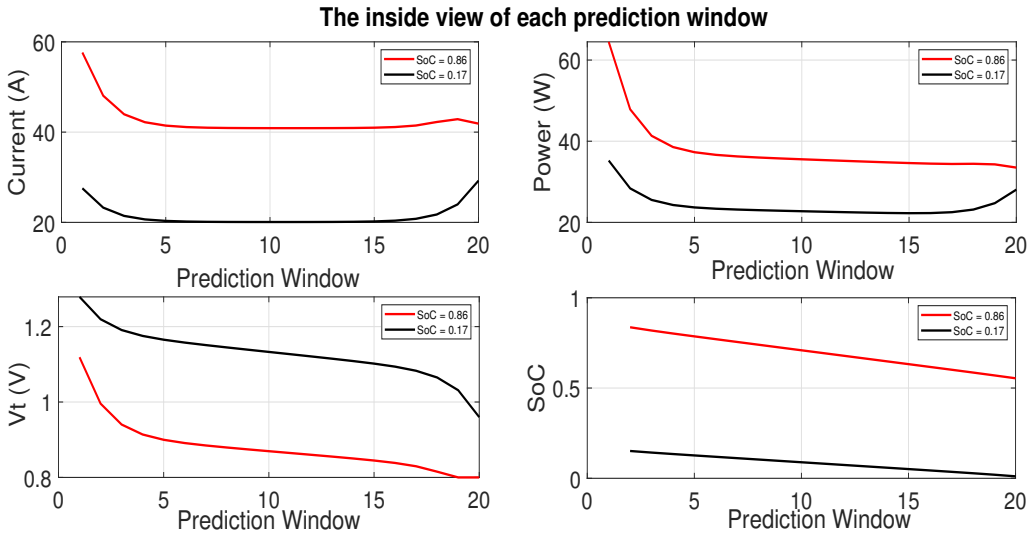

Figure 6: The inside view of each prediction window

5.2.2. Charging Phase

The proposed approach is also applied to the charging process, and the prediction results are briefly illustrated in Fig.7(a) and 7(b). Similarly, the cut-off voltage prevails in most cases, except for a longer prediction window and larger SoC states. When the prediction window >= 5, it is apparent that the value of predicted peak current decreases, resulting in drops in the predicted power. However, as the prediction horizon further increases, the predicted values are almost similar. At the beginning of the charging phase, due to lower SoC values, similar to the discharging phase discussion, the voltage constraints prevail as reflected in all the predicted values. As the charging proceeds, the effective constraints have been shifted from the voltage control to both the voltage and SoC controls. On the other hand, for long prediction windows, the instantaneous charging abilities are weakened. At the end of charging phase, the SoC control completely replace the voltage control, as shown in the fourth subplot of Fig.7(b). Therefore, it is essential to avoid overcharging at the end of the charging phase.

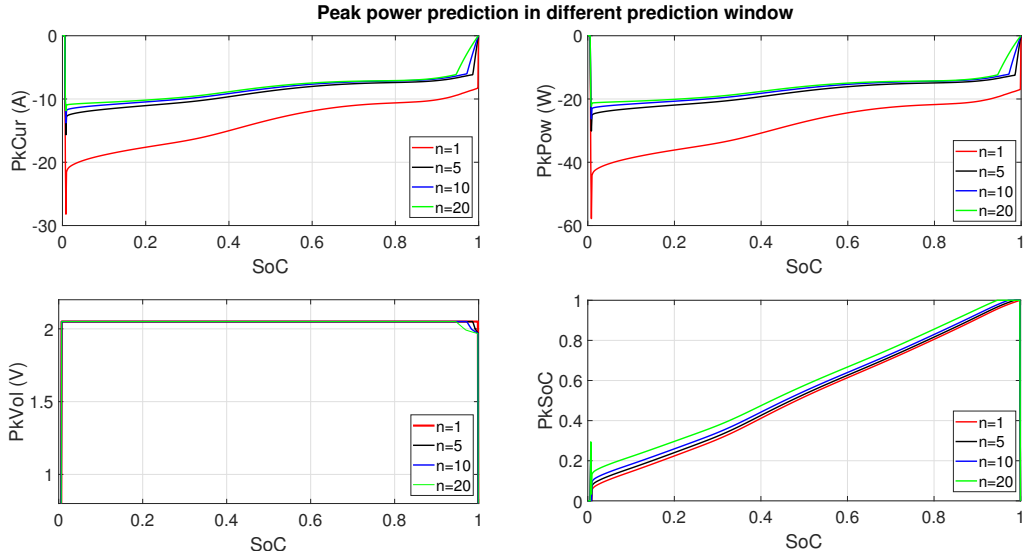

(a) Peak power prediction along the charging process

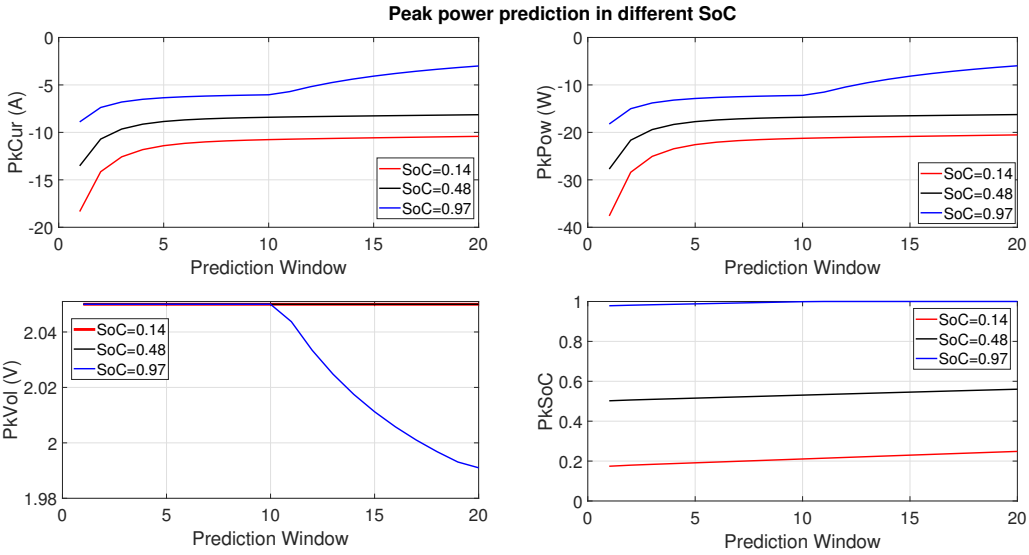

(b) Peak power prediction in different SoC states in the charging process

Figure 7: Peak power prediction for charging process

5.3. Discussions on the current and flow rate constraints

5.3.1. Current constraint

The used materials and the structure of ZNBs are two major limiting factors for applied current density on the surface of electrodes, thus the magnitude limit of the imposed current of the battery stack. Existing work reveals that the battery performance is bounded by the nonuniform zinc deposition and the oxygen evolution [13]. These side effects become more serious under higher applied current densities. Therefore, ZNBs have to be operated at low current densities (below $20mA/cm^2$) [10] in the past, which is not acceptable in the real applications. Much of the work that has been done so far in the literature mainly focuses on the development of new materials for the battery, and a continuous charge-discharge cycle test at $80mA/cm^2$ operating current density on a new material design shows that the average coulombic efficiency (CE) stays at 96% [22]. Similar promising results are also reported in other published work. The latest $Ni-3D\ Zn$ configuration [23, 15] has demonstrated fourfold increase in the applied current density, and the cost can be significantly reduced. Note that popular materials in RBFs used in existing batteries, including the one used in this study, are still not optimally designed. Given these considerations, only approximated current constraints are imposed in this study, for a bench-marking reference. Once the accurate constraints are confirmed, it can be readily integrated into Eq (21) according to the proposed algorithms. The detailed analysis is presented below for the ZNBs.

In this work, the N_iOOH sheets (positive electrode) and the stainless steels sheets (negative electrode) are stacked in parallel. Then, all the electrodes are machined into $7cm*7cm$ size. If the applied current density is set up as $80mA/cm^2$, the loaded current thresholds is then calculated as $80mA/cm^2 * 7cm * 7cm * 7 = 27.440A$, in which 7 individual cells are stacked in parallel. As illustrated in the second subplot of Fig.8, the predicted peak current is irrelevant to the current constraints in the charging phase, implying that in the charging phase, other constraints prevail over the acceptable bounds for the charging current.

On the other hand, in the discharging phase, the first subplot reveals that the situation is reversed. With the exception for small SoC ranges (between 0 to 0.2) over longer prediction horizons, other predicted peak current will be constrained by the material-determined cur-

rent threshold 27.440A. This implies that the state-of-the-art electrode materials are though far from the optimum, which is the main challenge of ZNBs. Nevertheless, even with this limitation, when compared with other RFBs, ZNBs still exhibit the highest instantaneous discharging peak power due to the relatively lower cut-off voltage (0.8V). As new materials are introduced, the material-determined current threshold 27.440 can be further relaxed.

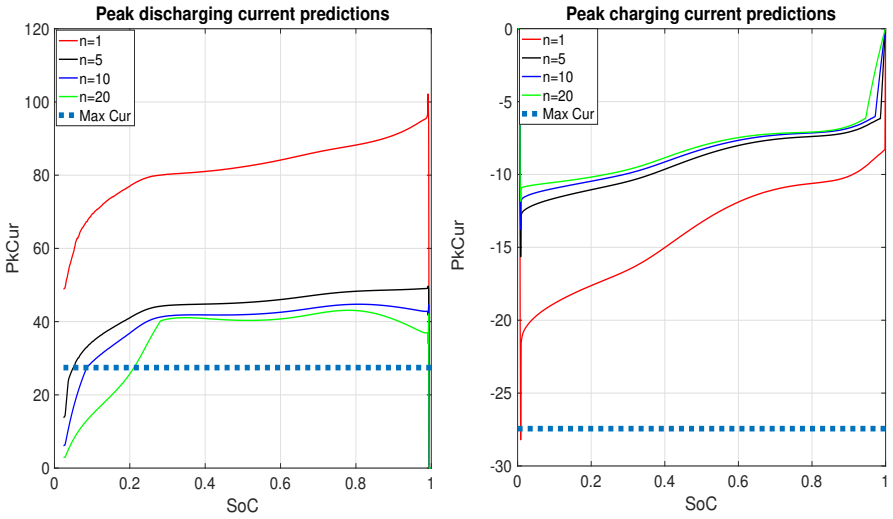

Figure 8: Predicted peak current considering material limits

5.3.2. Flow rate constraint

The electrolyte in ZNBs will take away the generated heat and moderate the thermal influence on the battery operations. The introduction of the flowing assisted system also helps to attenuate the dendrite formation [10, 11, 12]. As a consequence, the entire lifespan of ZNBs can meet the acceptable industry requirement. Therefore, the flow rate has a significant impact on the ZNB operation efficiency.

To achieve compact zinc deposition, the flowing velocity on the surface of electrodes should be sufficiently big to achieve steady convection control for the immigration reaction. The forced convection of the electrolyte close to the working electrodes will generate a constant thickness of the diffusion layer δ_N. Two widely accepted assumptions are taken into the consideration [43]:

* **Flow direction.** The flow direction is ideally in parallel to the electrode plates and perpendicular to the diffusion direction of the reactive ion.

* **laminated distribution.** The laminar flow of the electrolyte is assumed. As the presentation of friction, the flow velocity near the electrodes is zero. While the velocity maintains at the steady velocity u_0 far from the electrodes ($> \delta_{Pr}$).

Given the above assumptions, for the steady convection control of the reaction, the thickness of the diffusion layer δ_N can be formulated as [43]:

$$\delta_N \approx D^{1/3}\nu^{1/6}y^{1/2}u_0^{-1/2} \tag{26}$$

where D, y and ν are the diffusion constant, length of the plate, and viscosity coefficient of the supporting electrolyte ($10Mol \quad KOH + 1Mol \quad ZnO$), respectively. Therefore, the maximal tolerant current densities I_{lim} at a certain flowing velocity u_0 can be derived reversely:

$$I_{lim} = nFD\frac{c_0}{\delta_N} \approx nFD^{2/3}\nu^{-1/6}y^{-1/2}u_0^{-1/2}c_0 \tag{27}$$

where n is relative to the redox reaction for a given amount number of participated electrons. c_0 stands for the time-varying bulk concentration of zinc. F and δ_{Pr} represent the Faraday equation, namely the Faraday's constant and the thickness of Prandt's boundary layer, respectively. In a normal charging/discharging cycling, the concentration of zinc will be replenished or consumed with the progress of the redox reactions. As a consequent, the bulk concentration of zinc is SoC dependent variable and can be represented on the form:

$$c_0 = c_i - \frac{SOC(\%) \times C_{bat}(Ah) \times 3600}{nF \times V} \tag{28}$$

where V is the total volume of the electrolyte, and C_{bat} is the rated capacity of the battery. While c_i represents the initial zinc concentration.

Theoretically, the applied current densities are bounded by the flow rate and other inherent aspects as interpreted by Eq (27). In this work, the flow rate is large enough to eliminate the side influences. Note that in real applications, due to superbly high concentration of electrolytes applied, the subtle fluctuations of the concentration caused by the

redox reaction is negligible. Throughout the entire discharging and charging phases, the zinc concentration is varied slightly, rather stable. Thereby, the magnitude of the limited current densities I_{lim} is relative stable during the reactions. Due to Eq (27) and (28), the similar assumptions have also been applied to the analysis of other RBFs, and in this work, the current constraints incurred by the flow rate can be ignored in ZNBs.

6. Conclusion

This paper presents a novel peak power prediction approach for the Zinc Nickel single flow batteries. The RLS based real-time model identification process is first introduced to acquire an accurate battery model, thus the uncertainties incurred by different operating conditions can be addressed in real time. Then an EKF based SoC estimator is employed to acquire precise estimations which is confirmed in the experiments. With these preliminaries, a window-based peak power prediction framework is proposed which guarantees that the dynamics of current and voltage across the entire prediction windows are taken into the considerations. The proposed framework is capable of incorporating all the constraints on the current, voltage, and SoC that are satisfied. Experimental results confirm the effectiveness of the proposed scheme. Further, four indices are implemented to assess the power delivery/absorption capabilities of ZNBs while operation constraints are guaranteed. Finally, the influences of the material and flow rate on the peak power prediction are analysed qualitatively, proving a bench-marking paradigm in the RFBs research.

Acknowledgments

The authors would like to thank Dr. C.K. Wong and Miss YX. LI to provide the data and experimental resource supported by the Macao Science and Technology Development Fund under grant number 111/2013/*A*3 *(Flow Battery Storage System Study and Its Application in Power System).* S. Li would also like to thank Dr Peter Fischer from the Fraunhofer-Institut Chemische Technologie for helpful discussions. The work is partly funded by National Natural Science Foundation of China (NSFC) under grant 61673256, and State Key Laboratory of Alternate Electrical Power System with Renewable Energy Source under grant $LAPS17018$.

References

[1] P. Leung, X. Li, C. P. De León, L. Berlouis, C. J. Low, F. C. Walsh, Progress in redox flow batteries, remaining challenges and their applications in energy storage, Rsc Advances 2 (27) (2012) 10125–10156.

[2] P. J. Hall, E. J. Bain, Energy-storage technologies and electricity generation, Energy policy 36 (12) (2008) 4352–4355.

[3] A. Z. Weber, M. M. Mench, J. P. Meyers, P. N. Ross, J. T. Gostick, Q. Liu, Redox flow batteries: a review, Journal of Applied Electrochemistry 41 (10) (2011) 1137.

[4] M. Skyllas-Kazacos, M. Chakrabarti, S. Hajimolana, F. Mjalli, M. Saleem, Progress in flow battery research and development, Journal of The Electrochemical Society 158 (8) (2011) R55–R79.

[5] C. P. De Leon, A. Frías-Ferrer, J. González-García, D. Szánto, F. C. Walsh, Redox flow cells for energy conversion, Journal of Power Sources 160 (1) (2006) 716–732.

[6] P. Zhao, H. Zhang, H. Zhou, B. Yi, Nickel foam and carbon felt applications for sodium polysulfide/bromine redox flow battery electrodes, Electrochimica Acta 51 (6) (2005) 1091–1098.

[7] A. Shibata, K. Sato, Development of vanadium redox flow battery for electricity storage, Power Engineering Journal 13 (3) (1999) 130–135.

[8] Q. Lai, H. Zhang, X. Li, L. Zhang, Y. Cheng, A novel single flow zinc–bromine battery with improved energy density, Journal of Power Sources 235 (2013) 1–4.

[9] A. Hazza, D. Pletcher, R. Wills, A novel flow battery: A lead acid battery based on an electrolyte with soluble lead (ii) part i. preliminary studies, Physical Chemistry Chemical Physics 6 (8) (2004) 1773–1778.

[10] J. Cheng, L. Zhang, Y.-S. Yang, Y.-H. Wen, G.-P. Cao, X.-D. Wang, Preliminary study of single flow zinc–nickel battery, Electrochemistry Communications 9 (11) (2007) 2639–2642.

[11] Y. Cheng, H. Zhang, Q. Lai, X. Li, D. Shi, Performance gains in single flow zinc–nickel batteries through novel cell configuration, Electrochimica Acta 105 (2013) 618–621.

[12] L. Zhang, J. Cheng, Y.-s. Yang, Y.-h. Wen, X.-d. Wang, G.-p. Cao, Study of zinc electrodes for single flow zinc/nickel battery application, Journal of Power Sources 179 (1) (2008) 381–387.

[13] Y. Ito, M. Nyce, R. Plivelich, M. Klein, D. Steingart, S. Banerjee, Zinc morphology in zinc–nickel flow assisted batteries and impact on performance, Journal of Power Sources 196 (4) (2011) 2340–2345.

[14] Y. Ito, M. Nyce, R. Plivelich, M. Klein, S. Banerjee, Gas evolution in a flow-assisted zinc–nickel oxide battery, Journal of Power Sources 196 (15) (2011) 6583–6587.

[15] J. F. Parker, C. N. Chervin, I. R. Pala, M. Machler, M. F. Burz, J. W. Long, D. R. Rolison, Rechargeable nickel–3d zinc batteries: An energy-dense, safer alternative to lithium-ion, Science 356 (6336) (2017) 415–418.

[16] W. Waag, C. Fleischer, D. U. Sauer, Adaptive on-line prediction of the available power of lithium-ion

batteries, Journal of Power Sources 242 (2013) 548–559.

[17] G. Liu, M. Ouyang, L. Lu, J. Li, J. Hua, A highly accurate predictive-adaptive method for lithium-ion battery remaining discharge energy prediction in electric vehicle applications, Applied Energy 149 (2015) 297–314.

[18] R. Xiong, Y. Zhang, H. He, X. Zhou, M. G. Pecht, A double-scale, particle-filtering, energy state prediction algorithm for lithium-ion batteries, IEEE Transactions on Industrial Electronics 65 (2) (2018) 1526–1538.

[19] P. Shen, M. Ouyang, L. Lu, J. Li, X. Feng, The co-estimation of state of charge, state of health, and state of function for lithium-ion batteries in electric vehicles, IEEE Transactions on Vehicular Technology 67 (1) (2018) 92–103.

[20] L. Pei, C. Zhu, T. Wang, R. Lu, C. Chan, Online peak power prediction based on a parameter and state estimator for lithium-ion batteries in electric vehicles, Energy 66 (2014) 766–778.

[21] X. Qiu, T. A. Nguyen, J. D. Guggenberger, M. L. Crow, A. C. Elmore, A field validated model of a vanadium redox flow battery for microgrids, IEEE Transactions on Smart Grid 5 (4) (2014) 1592–1601.

[22] Y. Cheng, Q. Lai, X. Li, X. Xi, Q. Zheng, C. Ding, H. Zhang, Zinc-nickel single flow batteries with improved cycling stability by eliminating zinc accumulation on the negative electrode, Electrochimica Acta 145 (2014) 109–115.

[23] Y. Cheng, H. Zhang, Q. Lai, X. Li, D. Shi, L. Zhang, A high power density single flow zinc–nickel battery with three-dimensional porous negative electrode, Journal of Power Sources 241 (2013) 196–202.

[24] X. Li, K. Li, Z. Yang, C. Wong, A novel rbf neural model for single flow zinc nickel batteries, in: Advanced Computational Methods in Energy, Power, Electric Vehicles, and Their Integration, Springer, 2017, pp. 386–395.

[25] U. ABC, Us abc electric vehicle battery test procedures manual, revision 2, principal author: Gary Hunt, Idaho National Engineering Laboratory (INEL), US Department of Energy Idaho Field Office, DOE/ID-10479, Rev 2.

[26] F. Zheng, J. Jiang, B. Sun, W. Zhang, M. Pecht, Temperature dependent power capability estimation of lithium-ion batteries for hybrid electric vehicles, Energy 113 (2016) 64–75.

[27] G. L. Plett, High-performance battery-pack power estimation using a dynamic cell model, IEEE Transactions on Vehicular Technology 53 (5) (2004) 1586–1593.

[28] L. Zheng, J. Zhu, G. Wang, D. D.-C. Lu, T. He, Lithium-ion battery instantaneous available power prediction using surface lithium concentration of solid particles in a simplified electrochemical model, IEEE Transactions on Power Electronics.

[29] J. Meng, G. Luo, M. Ricco, M. Swierczynski, D.-I. Stroe, R. Teodorescu, Overview of lithium-ion battery modeling methods for state-of-charge estimation in electrical vehicles, Applied Sciences 8 (5)

(2018) 659.

[30] X. Hu, S. Li, H. Peng, A comparative study of equivalent circuit models for li-ion batteries, Journal of Power Sources 198 (2012) 359–367.

[31] Z. Wei, S. Meng, K. J. Tseng, T. M. Lim, B. H. Soong, M. Skyllas-Kazacos, An adaptive model for vanadium redox flow battery and its application for online peak power estimation, Journal of Power Sources 344 (2017) 195–207.

[32] Z. Wei, J. Zhao, B. Xiong, Dynamic electro-thermal modeling of all-vanadium redox flow battery with forced cooling strategies, Applied Energy 135 (2014) 1–10.

[33] Y. Zhang, J. Zhao, P. Wang, M. Skyllas-Kazacos, B. Xiong, R. Badrinarayanan, A comprehensive equivalent circuit model of all-vanadium redox flow battery for power system analysis, Journal of Power Sources 290 (2015) 14–24.

[34] X. Liu, Z. Chen, C. Zhang, J. Wu, A novel temperature-compensated model for power li-ion batteries with dual-particle-filter state of charge estimation, Applied Energy 123 (2014) 263–272.

[35] H. He, R. Xiong, H. Guo, S. Li, Comparison study on the battery models used for the energy management of batteries in electric vehicles, Energy Conversion and Management 64 (2012) 113–121.

[36] W. Waag, S. Käbitz, D. U. Sauer, Application-specific parameterization of reduced order equivalent circuit battery models for improved accuracy at dynamic load, Measurement 46 (10) (2013) 4085–4093.

[37] Z. Wei, J. Zhao, D. Ji, K. J. Tseng, A multi-timescale estimator for battery state of charge and capacity dual estimation based on an online identified model, Applied Energy 204 (2017) 1264–1274.

[38] R. Xiong, Q. Yu, L. Y. Wang, C. Lin, A novel method to obtain the open circuit voltage for the state of charge of lithium ion batteries in electric vehicles by using h infinity filter, Applied Energy 207 (2017) 346–353.

[39] Z. Wei, K. J. Tseng, N. Wai, T. M. Lim, M. Skyllas-Kazacos, Adaptive estimation of state of charge and capacity with online identified battery model for vanadium redox flow battery, Journal of Power Sources 332 (2016) 389–398.

[40] G. L. Plett, Extended kalman filtering for battery management systems of lipb-based hev battery packs: Part 3. state and parameter estimation, Journal of Power sources 134 (2) (2004) 277–292.

[41] J. Zhang, Y. Zhou, Y. Li, G. Hou, F. Fang, Generalized predictive control applied in waste heat recovery power plants, Applied energy 102 (2013) 320–326.

[42] H. N. Nguyen, P. O. Gutman, Fast constrained lqr based on mpc with linear decomposition, IEEE Transactions on Automatic Control 61 (9) (2016) 2585–2590.

[43] X. Li, C. Wong, Z. Yang, A novel flowrate control method for single flow zinc/nickel battery, in: Students on Applied Engineering (ICSAE), International Conference for, IEEE, 2016, pp. 30–35.